Acta Materialia 239 (2022) 118247

Contents lists available at ScienceDirect

Acta Materialia

journal homepage: www.elsevier.com/locate/actamat

On the formation mechanisms of intragranular shear bands in olivine by stress-induced amorphization

Hosni Idrissi[a,b,*], Armand Béché[b], Nicolas Gauquelin[b], Ihtasham Ul-Haq[b], Caroline Bollinger[c,#], Sylvie Demouchy[d,+], Johan Verbeeck[b], Thomas Pardoen[a], Dominique Schryvers[b], Patrick Cordier[e,f]

[a] Institute of Mechanics, Materials and Civil Engineering, UCLouvain, Louvain-la-Neuve, Belgium
[b] Electron Microscopy for Materials Science, University of Antwerp, Antwerp, Belgium
[c] Bayerisches Geoinstitut, Universität Bayreuth, D-95445 Bayreuth, Germany
[d] Géosciences Montpellier, Université de Montpellier and CNRS, UMR5243, Montpellier, France
[e] Univ. Lille, CNRS, INRAE, ENSCL, UMR 8207 - UMET - Unité Matériaux et Transformations, F-59000 Lille, France
[f] Institut Universitaire de France, 1 rue Descartes, F-75005 Paris, France

ARTICLE INFO

Article history:
Received 14 March 2022
Revised 22 June 2022
Accepted 4 August 2022
Available online 5 August 2022

Keywords:
Stress-induced amorphization mechansims
Shear band
Olivine

ABSTRACT

Intragranular amorphization shear lamellae are found in deformed olivine aggregates. The detailed transmission electron microscopy analysis of intragranular lamella arrested in the core of a grain provides novel information on the amorphization mechanism. The deformation field is complex and heterogeneous, corresponding to a shear crack type instability involving mode I, II and III loading components. The formation and propagation of the amorphous lamella is accompanied by the formation of crystal defects ahead of the tip. These defects are geometrically necessary [001] dislocations, characteristics of high-stress deformation in olivine, and rotational nanodomains which are tentatively interpreted as disclinations. We show that these defects play an important role in dictating the path followed by the amorphous lamella. Stress-induced amorphization in olivine would thus result from a direct crystal-to-amorphous transformation associated with a shear instability and not from a mechanical destabilization due to the accumulation of high number of defects from an intense preliminary deformation. The preferential alignment of some lamellae along (010) is a proof of the lower ultimate mechanical strength of these planes.

1. Introduction

Plastic deformation of crystalline solids is generally mediated by the motion of defects: point defects, dislocations or grain boundaries. Unlike these conventional deformation mechanisms, there is a growing body of evidence of deformation made by atomic scale amorphous band formation in ceramics [1–5] and in other covalently bonded solids like semiconductors [6–9] subjected to shocks or deformed at low temperature (for example by indentation). Originally, solid-state amorphization has been mostly considered as a response to pressure [10,11] and interpreted on the basis of thermodynamics and of mechanical stability arguments [12,13]. A kinetically preferred transformation path is proposed to arise due to a frustration in the attainment of the high-pressure equilibrium crystalline state. The efficiency of shear in promoting amorphization at lower pressures was however early recognized [14] and led to considering stress-induced amorphization as a deformation mechanism [9,15–18]. However, the elementary mechanisms driving the amorphization as well as its links with the other deformation mechanisms still need to be clarified.

Ovid'ko [19] distinguishes two possible classes of amorphization induced deformation mechanisms. In the first case, amorphization is an ultimate stage of plasticity and results from a structural collapse related to an accumulation of crystal defects [20]. This is the mechanism envisaged for metals with a sufficient ductility. For example, Koike *et al.* [21] observed the amorphization of a NiTi alloy rolled at room temperature. The microstructural analysis

* Corresponding author at: IMAP - Materials and Process Engineering, iMMC - Institute of Mechanics, Materials and Civil Engineering, Bat. Réaumur - b.114, L5.02.02, Place Sainte Barbe 2, 1348 Louvain-la-Neuve, Belgium.
E-mail address: hosni.idrissi@uclouvain.be (H. Idrissi).
Now at IRAP, Université de Toulouse, CNRS, CNES, UPS, F- 31400 Toulouse, France
+ Now at: Laboratoire Magmas et Volcans, Université Clermont Auvergne, CNRS, IRD & OPGC, UMR 6524, 63170 Aubière, France.

https://doi.org/10.1016/j.actamat.2022.118247

revealed very high dislocation densities 10^{17}-10^{18} m^{-2} in the vicinity of amorphous areas. Based on the estimation that the elastic energy arising from this dislocation density is of the same order as the crystallization energy, Koike *et al.* concluded that dislocation accumulation is the major force driving the amorphization in cold-rolled NiTi [21]. The role of dislocations is however not limited to ductile crystals. In superhard boron suboxide (B_6O) subjected to nanoindentation, the observation of dislocation loops next to amorphous bands led Reddy *et al.* to relate the collapse of the crystal lattice to the accumulation of dislocations during shear sliding [22]. This model has been again applied recently by Reddy *et al.* to account for amorphization in B_4C [23]. A similar conclusion was reached by Lin *et al.* [24] for monoclinic γ-$Y_2Si_2O_7$, a refractory ceramic indented at room temperature, based on striking similarities between the organization and properties of amorphous layers, and the one of slip bands containing dislocation pile-ups. The role of dislocations has also been proposed to account for the amorphization of covalent solids. The observation in electron microscopy of ball-milled silicon [25] has shown that amorphization initiates along defects (dislocations, stacking faults). This mechanism has been confirmed since then [26] with however some discussions about the possible implication of some intermediate phase (diamond-hexagonal, see He *et al.* [8]). In a molecular dynamics-based numerical study, Chen *et al.* [27] considered, like Lin *et al.* [24], the amplifying role that dislocation pile-ups can play in triggering silicon amorphization. Besides dislocations, the role of elastic distortions at disclinations has been discussed from a theoretical point of view, in particular for disclination quadrupoles in deformed nanomaterials [16].

The second case of amorphization, proposed by Ovid'ko [19] considers the possibility that amorphization directly results from an elastic instability under high stress when other deformation mechanisms are inhibited [9]. There are indeed many experimental evidence of amorphization without the prior formation or accumulation of crystal defects. This is the case for example of the quartz micropillars drawn during *in situ* deformation in a transmission electron microscope [28]. In the intermetallic $SmCo_5$, Luo *et al.* demonstrated by molecular dynamics (MD) simulations that plastic deformation can be produced through the formation of amorphization shear bands without the need of dislocations [29].

This study addresses the stress-induced amorphization of olivine, the main constituent of the upper mantle of the Earth, which may contribute to the viscosity drop at the lithosphere-asthenosphere boundary [30]. Olivine is known to be very difficult to vitrify by melt quenching [12]. The first report of amorphization of olivine has been made by Jeanloz *et al.* [31] in shocked samples recovered from peak pressure of about 56 GPa (see also recent report of amorphization shear bands in shocked olivine from Zhao *et al.* [9]). The contribution of stress-induced amorphization to plastic deformation of olivine has first been reported in single crystal micropillars deformed in compression [32] at room pressure and temperature. Then Samae *et al.* [30] reported pervasive occurrence of amorphization along grain boundaries in specimens deformed at low temperature, *i.e.* below 1200 °C [30]. This stress-induced amorphization of grain boundaries was shown to strongly promote grain boundary sliding. Apart from the fact that the latter study highlighted that amorphization occurred preferentially along planar defects (grain boundaries), it did not allow conclusions to be drawn as to the amorphization mechanism itself. In the present study, we further investigate the samples of Samae *et al.* [30] by transmission electron microscopy (TEM) and by focusing on amorphous intragranular lamellae not previously described. We pay particular attention to a lamella which stops within a grain. The detailed examination of this interrupted propagative event allows us to study the formation of this amorphous lamella and to shed some light on its structural environment and thus on the mechanisms responsible for stress-induced amorphization in olivine.

2. Materials samples and experimental methods

The specimens come from two previous, independent studies by Bollinger *et al.* [33] and Gasc *et al.* [34]. The deformation conditions are summarized in Table 1. Specimen NF1050-1 was deformed by Gasc et al. [34] in a high-resolution gas-medium high-pressure deformation apparatus [35] which allows axial compression tests at high temperature (up to 1600 K) under a confining pressure of 300 MPa using argon gas. With this device, the axial force is measured during deformation with an internal piezo-resistivity load cell yielding high resolution stress-strain curves (by minimizing friction, which lead to uncertainty on the differential stress less than 20 MPa). A constant displacement rate was set based on the initial length of the sample to yield a stress plateau with a strain rate of 10^{-5} s^{-1}. Since the confining pressure applied by this gas-medium apparatus is small compared to mantle pressure, and to ensure that amorphization is not inhibited at high pressure, we have also characterized specimens (here we describe M628 only) deformed by Bollinger et al. [33] at 5 GPa (corresponding approximately to a depth of 140 km). To perform deformation experiments in this pressure range, a large volume multi-anvil system with employs six independently acting hydraulic rams [36] was used. This press is designed to perform deformation experiments using cubic solid pressure-media compressed between six square-faceted anvils that could each be moved independently. The maximum attainable sample pressure depends on the edge length dimension of the anvils. The high-pressure cell contains a heater which allows high-temperature experiments up to ca. 2000 K and the temperature is monitored with a thermocouple. For stress and strain to be measured, the press must be operated on a synchrotron beamline. This is not the case here so the stress is unknown and the strain is only qualitatively estimated from the displacement of the anvils.

In order to perform TEM analysis, the specimens were first mechanically polished down to a thickness of 30 μm. The sample foils mounted on Mo or Cu grids were Ar-ion sputtered with a Gatan DuoMill model 600 to reach electron transparency. In case of specimens deformed in the multi-anvil press, a final polishing was performed during a few minutes at grazing angle with a Gatan PIPS II model 695. A thin carbon layer was deposited to ensure electron conduction on the thin foils. Conventional high resolution TEM (HRTEM) images were acquired using a FEI Osiris at an operating voltage of 200 kV (Antwerp) and with a FEI Tecnai-G^2-20 twin microscope operating at 200 kV with a LaB_6 filament (Lille). HRTEM and high-resolution scanning TEM (STEM) imaging was also performed on the *QuanTEM*, a FEI Titan^3 microscope, operating at a 300 kV acceleration voltage and equipped with both TEM and STEM aberration correctors (Antwerp). High resolution high-angle-

Table 1
Summary of the deformation conditions. For experiments performed in the six-ram press, the final strains are estimated from the displacements of the pistons while the stress is not measured.

Ref sample	Apparatus	Pressure (GPa)	Temperature (°C)	Final strain (%)	Final stress (MPa)
NF1050-1 [34]	Paterson press	0.3	1050	10.4	1140
M628 [33]	Six-ram press	5	1200	20	-

annular-dark field scanning TEM (HAADF-STEM) images were acquired using a convergence semi-angle α of 22 mrad and 25 pA probe current, the ADF inner acceptance angle β and the Electron energy loss spectroscopy (EELS) acceptance angle were both equal to 28 mrad. The strain field surrounding the extended defects is mapped out using the geometrical phase analysis (GPA) approach. The GPA maps were calculated using an in-house software based on the work from Hÿtch et al. [37] and Rouvière et al. [38]. The edges of the mask used for the selection of the FFT spots were Gaussian smoothed to prevent influence from the sharp edges in the reconstructed GPA images. The selected Fourier spots and the position of the mask are systematically drawn in the experimental images. EELS was conducted with the same microscope equipped with a Gatan K2 Summit camera placed at the back of a Quantum GIF. For these measurements, the microscope was operated at 300 kV in the monochromated mode, providing an energy resolution of 150 meV. A beam current of 30 pA was selected to limit the beam induced damage and a large collection angle, increasing the EELS signal intensity, was allowed by the use of the EFSTEM camera lengths. An energy dispersion of 0.25 eV/pixel was used with an exposure time of 0.2 s/pixel at 100 % duty cycle of the K2 summit camera. The K2 camera keeps the energy resolution to 1 pixel (0.25 eV) thanks to its direct electron detection capability in counting mode, allowing a greatly improved direct quantum efficiency (DQE) compared to standard CCD sensors. Subsequently, the region corresponding to the EELS spectrum imaging was also imaged in HRTEM to confirm the absence of beam damage on the area of interest. The sensitivity to the electron beam of the olivine samples used in the present work was more marked in the STEM mode (compared to the TEM mode). HAADF and ABF-STEM conditions were simultaneously applied at low electron dose (the first one allowing quick contrast assessment, the second improving the image contrast compared to HAADF-STEM for a similar dose). This explains the noise in the images compared to other materials with higher stability under the electron beam such as in ceramics or metals. However, this did not hinder extracting relevant information regarding the mechanisms controlling stress induced amorphization in this material as shown hereafter.

3. Results of TEM analysis

Evidences of stress-induced amorphization at grain boundaries were reported in [30], and proposed to be responsible for promoting grain boundary sliding at *ca.* 1050 °C. Here we show that, in the same samples, some intragranular amorphous lamellae are also observed. These lamellae are mainly found in the samples of Bollinger *et al.* [33] deformed at 5 GPa, but also, though very occasionally, in the samples from Gasc *et al.* [34]. These intragranular amorphous lamellae are generally very thin (a few nanometers as shown in the HAADF-STEM images of Figs. 1a and 1b from the sample NF1050-1 deformed at 1050°C). The inverse FFT (IFFT) with 002 in the lower right inset of Fig. 1a confirms the shearing of these planes across the lamella. The sample M628 deformed at 1200 °C shows an intracrystalline deformation microstructure with dislocations but there is no apparent relationship between the microstructure of the amorphous lamellae and that of the dislocations (see the dark field TEM image of Fig. 1c). In particular, we see no indication that amorphous lamellae result from dislocation accumulations. This important finding was previously reported by Samae *et al.* [30] with respect to amorphous grain boundaries. Some lamellae show crystallographic control (facets in Fig. 1d) with preferential orientation close to (010) habitus, but this is not a strictly respected rule.

The EELS spectra of the O-*K*-edge in the crystal and in the shear band (Fig. 1e) are in perfect agreement with recently published XANES results on crystalline and amorphous forsterite respectively [39]. The radiation-induced peak at 530 eV (marked with an *) is from O_2 liberated during damage by the incident electron beam

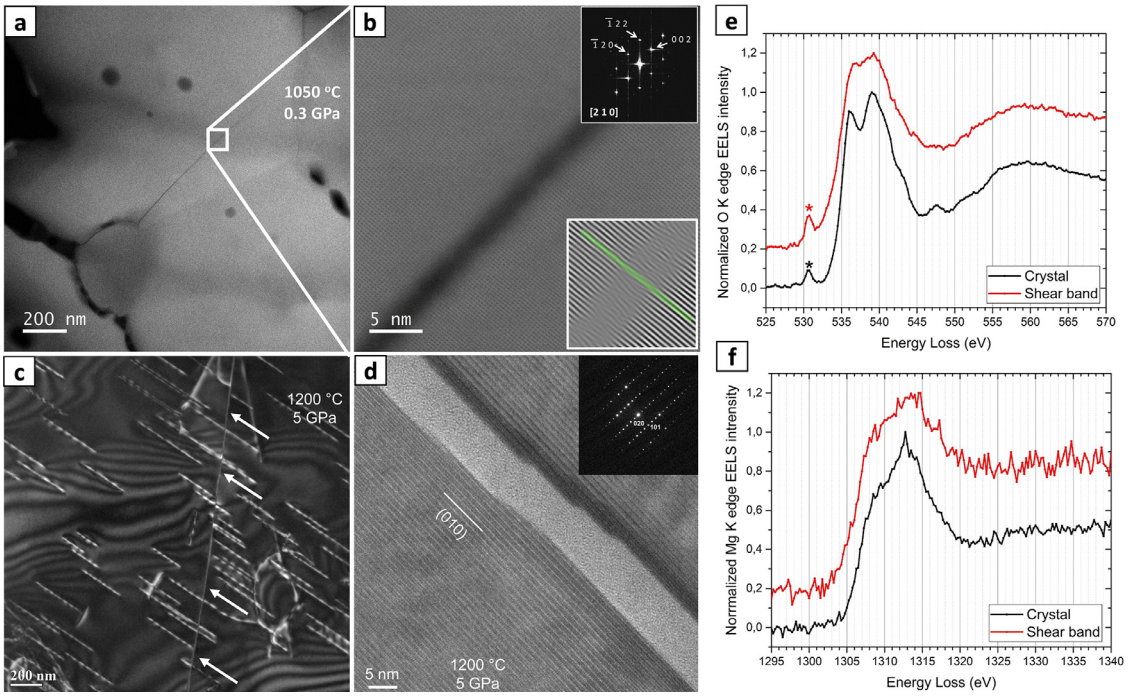

Fig. 1. Intragranular amorphization shear bands in olivine. (a) HAADF-STEM image of a shear band nucleated from a GB triple junction and stopping inside the grain in the sample deformed at 1050 °C and 0.3 GPa. (b) Zoom from the white square in (a) showing the amorphous nature of the band. The FFT in the top right inset shows the indexation of the zone axis while the IFFT with 002 in the lower right inset confirms the shear of these planes across the lamella. (c) Diffraction contrast dark-field TEM image showing an amorphization shear band in the sample deformed at 1200°C and 5 GPa. There is no relationship between the dislocation microstructure and the shear band. (d) HRTEM image from (c) showing the presence of steps along the band. (e) and (f) EELS spectra of the O-K-edge and Mg-K-edges, respectively, in the crystal and in a shear band.

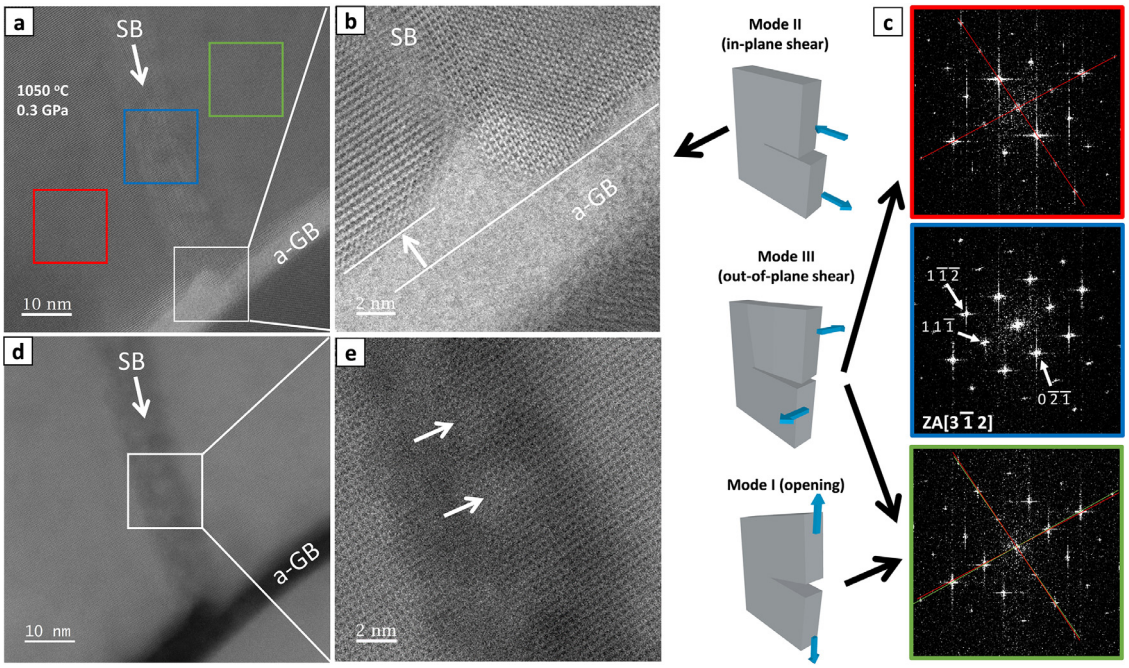

Fig. 2. Characterization of the displacement field induced by an amorphization shear band in the NF1050-1 sample deformed at 1050 °C. (a) High resolution ABF-STEM image on the nucleation of an amorphization shear band from the edge of an amorphous GB. (b) Zoom from the white square in (a) showing the amplitude and direction of the in-plane shear at the nucleation site (mode II). (c) Three FFTs from the red, blue and green squares in (a). The rotation of the spots in the red and green FFTs (see the red and green lines in the lower panel) confirms the presence of mode I while the difference of the intensities of the spots in these FFTs is in agreement with out-of-plane shear (mode III). (d) HAADF-STEM image of the same region in (a). (e) Zoom from the white square in (d) showing the presence of structural heterogeneities within the band.

[40] and was also detected in the XANES study mentioned earlier. The Mg-*K*-edges in Fig. 1f are similarly in agreement with crystalline and amorphous forsterite investigated by XANES. In conclusion, the EELS measurements confirm that the shear bands are predominantly made of amorphous olivine (note that identical EELS data were collected on the amorphous intergranular layers).

The high-resolution ABF-STEM image of Fig. 2a shows an amorphization shear band (SB) that has been thoroughly characterized in specimen NF1050-1 deformed at 1050°C. This SB originates from the edge of an amorphous grain boundary ("a-GB" in Fig. 2a) and ends in the interior of the grain as will be shown later. Note that, it was not possible, here, to orient the band edge-on while aligning the crystal in zone axis condition. The band of Fig. 2a is thus inclined with respect to the average plane of the foil which makes its characterization difficult. Fast Fourier Transforms (FFTs) have been performed on both sides of the band but also on the overlapping region (Fig. 2c). These FFTs show misorientations in the plane of the foil (~1-2°), but also out of the plane (visible from the differences in the intensity of the spots). If we add the shift of *ca.* 2 nm at the origin of the band (Fig. 2b), a complex displacement field shows up associated with this shear band. The three loading modes I, II and III, usually considered for cracks are involved (see the schematics of Fig. 2). Fig. 2d is a HAADF-STEM image of the same region as in Fig. 2a. It shows a darker contrast at the band due to the presence of the low-density amorphous phase resulting in absence of electron channeling. Furthermore, contrast variations observed within the inclined band (Fig. 2e) suggest that the displacement field is not constant along the band leading to different degrees of amorphization.

The ABF-STEM image of Fig. 3a shows the same band as in Fig. 2, but in a region far from the nucleation site. At this location, the band is aligned almost parallel to the electron beam, allowing for direct detection of some amorphous material at the band (FFT-1 of Fig. 3a). Interestingly, we note a splitting of the $\bar{1}\bar{1}1$ spot

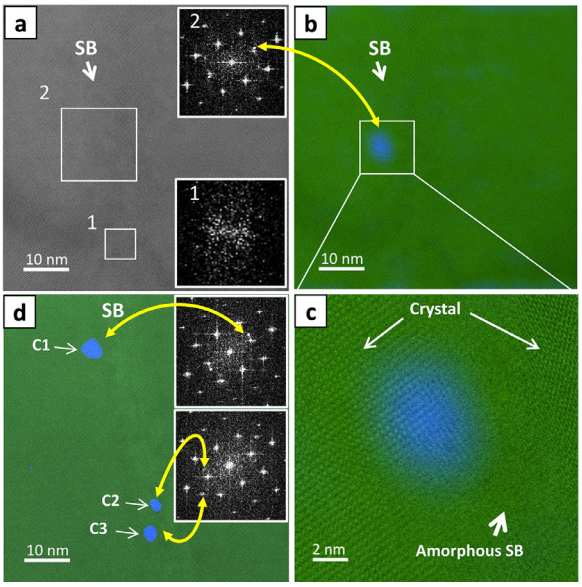

Fig. 3. Observation of rotational nanodomains along the amorphization shear bands of Fig. 2. (a) High resolution ABF-STEM image not far from the tip of the band viewed nearly edge-on. The FFT from square-1 in (a) shows the amorphous character of the band while the FFT from square-2 shows the splitting of the $\bar{1}\bar{1}1$ spot. (b) Superposition of the ABF-STEM image in (a) with a virtual dark field map with the extra spot. It shows the position of the rotational nanodomain associated to this spot along the band. (c) Zoom from the white square in (b) showing that the nanodomain is located at the interface between the crystal and the amorphization shear band. (d) The same procedure was used in a neighboring area of the same shear band. It shows the presence of 3 rotational nanodomains linked to three different spots in the FFTs of (d).

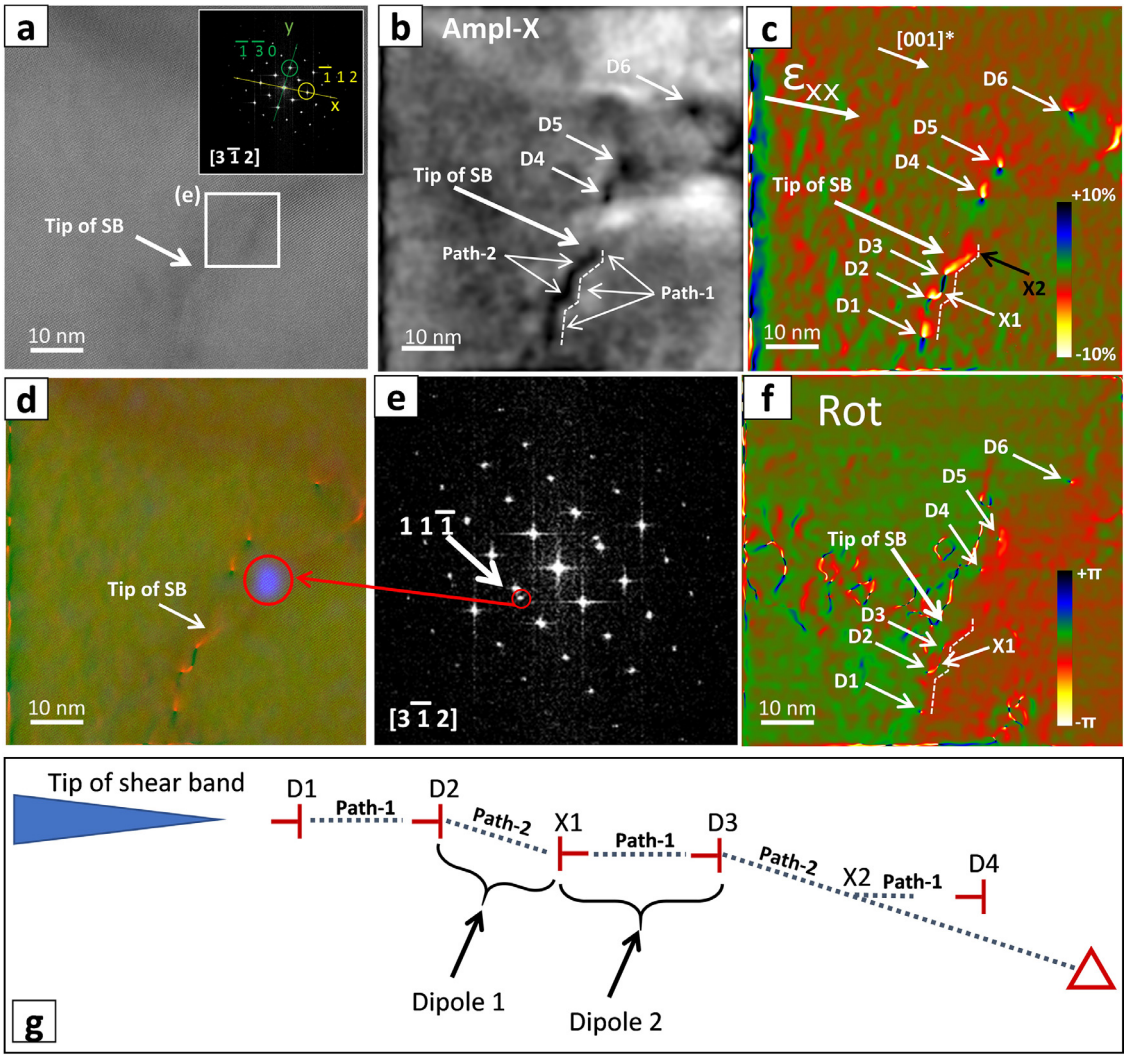

Fig. 4. Characterization of the propagation mechanisms of the shear band of Fig. 2. (a) High resolution ABF-STEM image at the tip of the shear band. (b) The GPA amplitude map corresponding to the $(\bar{1}\bar{1}1)$ plane in (a) showing the tip of the band and some dislocations ahead of the tip. Note that the tip follows two different paths. (c) GPA strain map ε_{xx} of (a), X corresponds to the $[\bar{1}12]$ direction and Y corresponds to the $[\bar{1}\bar{3}0]$ direction. It shows the presence of three dislocations at the tip of the SB (D1-D2-D3) and three other dislocations (D4-D5-D6) ahead of the tip. (d) Superposition of the ABF-STEM image in (a) with the GPA map of (c) and a virtual dark field map with an extra $\bar{1}\bar{1}1$ spot in the FFT of (e). This FFT belongs to the white square in (a). (d) Confirms the presence of a rotational nanodomain ahead of the tip of the shear band along Path-2. (f) GPA rotation map from (a). It shows that the six dislocations (D1-D6) are located at the interface between two regions with rigid in-plane rotation. (g) Schematic illustration showing the mechanisms controlling the propagation of the shear band based on the observations shown in (a-f), see the discussion section for more details. The red triangle represents a disclination possibly at the origin of the nanodomains.

(FFT-2 of Fig. 3a) which originates from a small domain (<5 nm) affected by a rotation of this lattice plane; see the overlap of the ABF-STEM image with a virtual dark field image using the spot of the domain affected by this rotation in Fig. 3b. Fig. 3c reveals that this nanodomain is located at the crystal/amorphous interface. Fig. 3d shows the superposition of an ABF-STEM image (acquired in a region very close to the one of Fig. 3a), in green, with three virtual dark field images, in blue, using FFT spots corresponding to three different nanodomains (C1, C2 and C3). It confirms that these nanodomains are frequently associated with the shear band, and were almost systematically observed in all pictures along the shear band. Note that C1 and C2 are linked to the splitting of the $\bar{1}\bar{1}1$ spot similar to Fig. 3b but with rotations in opposite directions while the origin of C3 cannot be elucidated in this crystal orientation. No similar nanodomains were observed away from the shear bands.

The displacement field ahead of the tip of the band (BF-STEM image of Fig. 4a) has been characterized in detail. In order to facilitate the observation of this tip, the amplitude map corresponding to the $(\bar{1}\bar{1}1)$ plane in the image of Fig. 4a is shown in Fig. 4b. In this map where dark contrast corresponds to regions with less frequency (blurring or absence of the $(\bar{1}\bar{1}1)$ planes) due to the amorphous band, it can be observed that the tip of the band exhibits a zig-zag morphology with the presence of three dark spots (D4, D5 and D6) ahead of the tip. These spots can be identified as dislocations in the GPA strain map ε_{xx} of Fig. 4c (where "X" corresponds to the $[\bar{1}12]$ direction). In this map and the rotation map of Fig. 4f, a few other dislocations (D1, D2 and D3) can also be identified near the SB tip. Both the amplitude map of Fig. 4b and the GPA strain map ε_{xx} of Fig. 4c confirm that these dislocations dictate the propagation path of the band as will be discussed in the next section.

All the dislocations (D1-D6) were characterized as [001] dislocations since they do not exhibit strain field contrast in the GPA strain map ε_{yy} ("Y" corresponds to the $[\bar{1}\bar{3}0]$ direction), see Fig. 5. Furthermore, in the GPA rotation map of Fig. 4f, it can be seen that the D1-D6 dislocations are located at the interface between two regions with rigid in-plane rotation. This indicates that these dis-

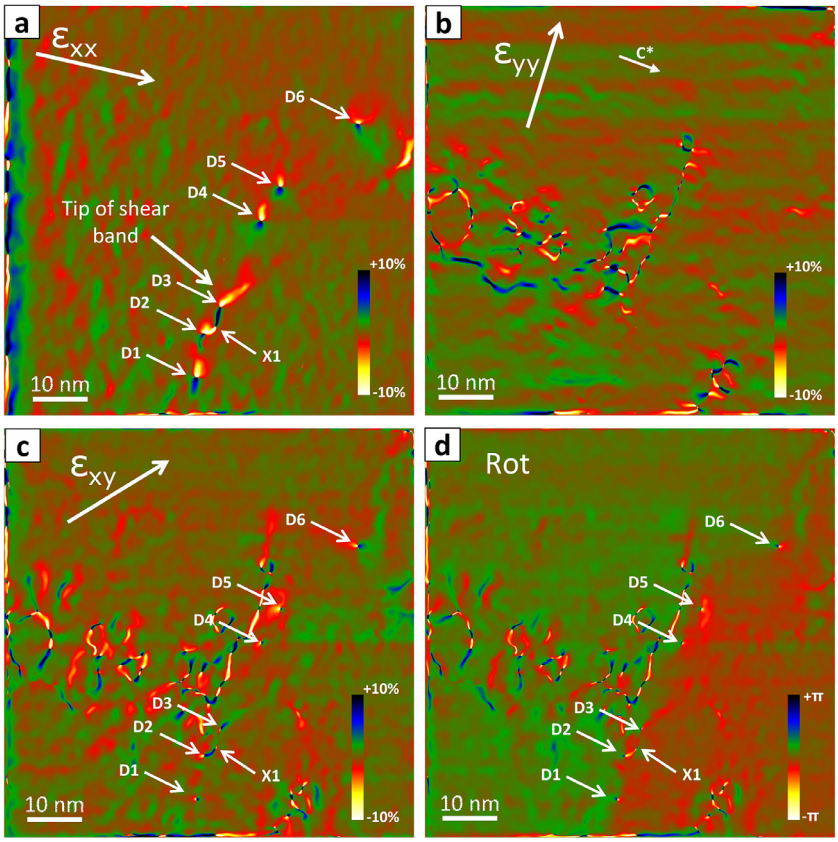

Fig. 5. Characterization of the Burgers vector of the dislocations at the tip of the shear band. (a, b, c and d) GPA strain maps ε_{xx}, ε_{yy}, ε_{xy} and rotation map, respectively from image (a) in Fig. 4, X corresponds to the $[\bar{1}12]$ direction and Y corresponds to the $[\bar{1}\bar{3}0]$ direction. Note the absence of the strain of dislocations D1-D6 and X1 in the GPA strain map ε_{yy} indicating that these dislocations are [001] dislocations.

locations have been nucleated in order to accommodate the large strain gradients ahead of the tip and could thus be considered as geometrically necessary dislocations (GNDs). Here again, we note ahead of the tip a splitting of the $\bar{1}\bar{1}1$ spot (see the FFT of Fig. 4e obtained from the white square in Fig. 4a). In Fig. 4d, this splitting corresponds to a small domain (∼5 nm) involving slight lattice plane rotations (∼11°), similar to the nanodomains shown in Fig. 3. However, it can be seen in Fig. 4d that this domain is not linked to the dislocations ahead of the tip. In the next section, attempts are made to explain such phenomena.

4. Discussion

The observations presented in the previous section shed new light on the mechanisms responsible for the localized stress-induced amorphization of olivine, in particular on the role of crystal defects, which is at the core of intense debates in the literature. Grain boundaries should be considered separately and will not be discussed in this paper. Microstructural investigations of the samples of Gasc *et al.* [34] and Bollinger *et al.* [33] as described in [30] show that grain boundaries concentrate most of the amorphization. Here, the interest is on unravelling the mechanisms at the origin of the intragranular amorphous lamellae. Some evidence of shear lamellae resulting from stress-induced amorphization were recently reported in olivine in single crystals micropillars compressed at low temperature [32] or in shock recovered samples [9] but no information was provided regarding the deformation mechanism. The detailed observation in our specimen of the tip of a lamella interrupted inside the core of a grain provide novel information to elucidate the local amorphization mechanism.

Fig. 4g shows a schematic illustration of the defects characterized ahead of the tip of the amorphization shear band. The high stresses and strain gradients lead to the nucleation of [001] GNDs (Fig. 4f). These dislocations apparently nucleate *ex nihilo* since their emission from the SB tip can be excluded. Indeed, their Burgers vector point perpendicular to the line connecting the tip and the GNDs (Path-1 in Figs. 4b and 4c). The high stress conditions lead to amorphization by the creation and extension of disorder from the SB tip down to the dislocation nucleated ahead from the tip (Path-1 from D1 to D2). However, because the next dislocation D3 is not located along Path-1, the band tip deviates to Path-2 and re-deviates to Path-1 when it approaches dislocation D3. In this case, a $[00\bar{1}]$ dislocation can be observed when the tip changes its path between D2 and D3 (dislocation X1 in Figs. 4c, 4f and 4g). This dislocation forms a dipole with dislocations D2 and D3. Dislocations similar to X1 are not observed close to the other GNDs D4, D5 and D6 far from the tip, indicating that this dislocation is associated with the change of the band path close to D3. Deviation from Path-1 to Path-2 also occurred at D3. In this case, dislocation D4 is quite far and the GPA strain map ε_{xx} of Fig. 4c shows that the maximum tensile strain direction at D3 is parallel to Path-2. It is also worth noting that the $\bar{1}\bar{1}1$ nanodomain is located along Path-2 from D3 quite far from the tip (Fig. 4d). Again, once the tip approaches a new [001] GND dislocation (D4), it starts deviating from Path-2 to Path-1. Indeed, a black arrow indicates a slight increase of the tensile strain direction towards D4 in the GPA map of Figs. 4c. This is probably the 'interrupted' nucleation site of new dipoles similar to those involving D2, D3 and X1 (position X2 in Figs. 4c and 4g).

These observations show that the band propagates by two mechanisms:

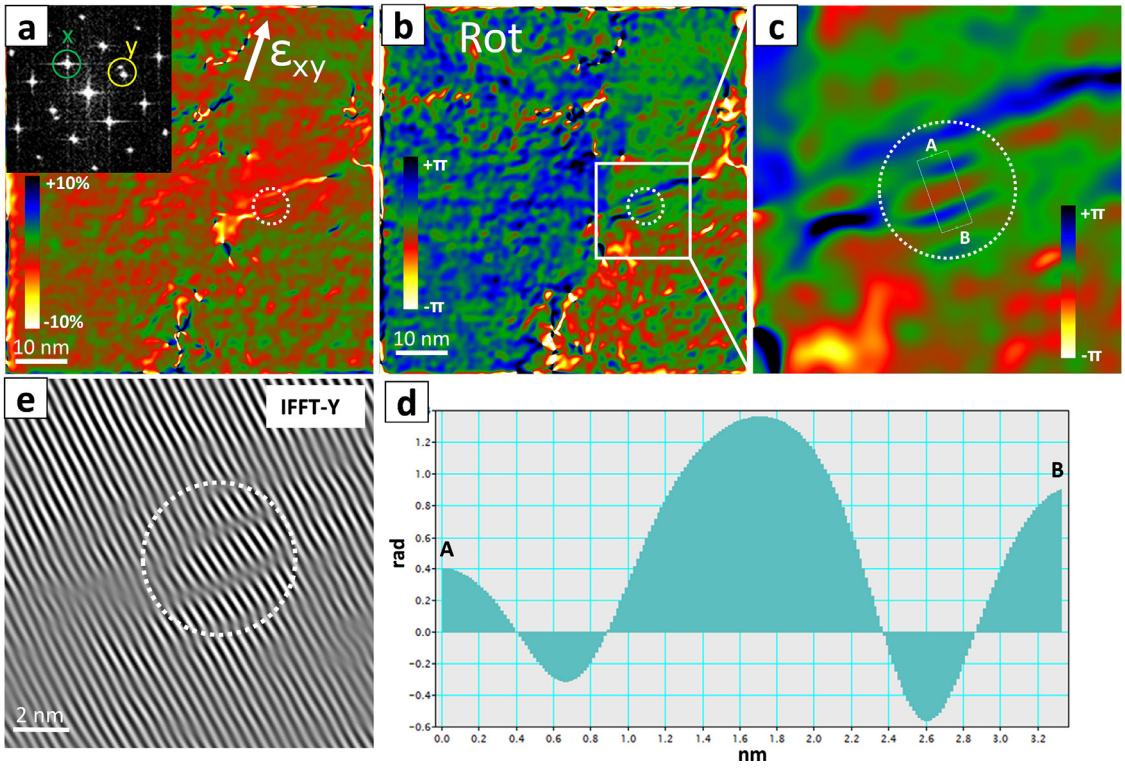

Fig. 6. Characterization of the nature of the rotational defect at the tip of the band in Fig. 4d. (a) and (b) GPA shear strain ε_{xy} and rotation maps from Fig. 4a, respectively ('X' corresponds to 021 while 'Y' corresponds to the two to $\bar{1}\bar{1}1$ splitting spots). The white dashed circles in Figs. 6a and 6b indicate the position of the nanodomain shown in Fig. 4d. (c) zoom from the white circle in (b) showing rotational fringes at the position of the nanodomain. (d) Line profile from the rectangle inside the white circle in (c). It shows that the fringes are associated to gradients with apposite sign. (e) Inverse FFT map obtained with the two $\bar{1}\bar{1}1$ splitting spots.

i) the formation of [001] GNDs in order to accommodate the large strain gradients in the region near the tip of the band. This is followed by the creation and extension of disorder between these dislocations along a specific direction parallel to the extra half plane of the GNDs (Path-1). The SB propagates towards the dislocations in order to minimize the elastic energy by amorphization.
ii) when the neighboring GND is far from the tip, the band tip can deviate into a second path (Path-2) which is probably imposed by the macroscopic stress. This is accompanied by the formation of a new defect involving local rotation of the lattice but far from the tip similar to what occurs during ductile fracture.

The nature of this new defect is intriguing since it induces a local rotation of specific planes while the other planes are not affected (see FFTs in Figs. 3 and 4). The local rotational field being affected, we will explore the possibility that this indicates the presence of a disclination. Figs. 6a and 6b show the GPA shear strain ε_{xy} and rotation maps, respectively (here 'X' corresponds to the [021] direction while 'Y' corresponds to [$\bar{1}\bar{1}1$] direction). Note that the mask used to select 'Y' also includes the second spot of the rotated $\bar{1}\bar{1}1$ plane. The white dashed circles in Figs. 6a and 6b indicate the position of the nanodomain shown in Fig. 4d. In these two figures, fringes related to this nanodomain can be observed in the shear and rotation maps. These fringes correspond to rapidly oscillating field. Such fringes can also be observed in the inverse FFT map obtained with the two $\bar{1}\bar{1}1$ splitting spots (Fig. 6e), here indicating a strong phase shift in the geometrical phase. Interestingly, the line profile from the rotation map in this area (Figs. 6c and 6f) shows that the fringes are associated with gradients of opposite signs. A local, anisotropic, rotation field is an indication (in the absence of an alternative hypothesis) of a disclination type defect.

The observation of the nucleation of defects (dislocations and possibly disclinations) *ex nihilo* ahead of the tip of the band shows that locally the stresses can be so strong that the perfect crystal becomes structurally unstable leading to the local formation of discontinuities of the displacement or rotation fields. The non-uniform stress field ahead of the tip of the band leads to the nucleation of defects, then the deformation fields of these defects direct the propagation of the band. This mechanism reflects conditions where the stress cannot be locally relaxed by classical plasticity mechanisms. This can be explained by the fact that the local stress field does not find the slip systems needed in this low symmetry mineral. It can also be for kinetic reasons if the local strain-rate is too high for these mechanisms to be activated.

We find that, in olivine, defect formation accompanies amorphization, but that, contrary to what several recent studies suggest, especially in covalent or high lattice friction materials, amorphization cannot be considered as a consequence of defect accumulation.

We observe ahead of the propagating amorphous shear lamella evidences of very high stresses reaching the theoretical elastic limit causing the nucleation of defects and lattice instability. The DFT calculations of Gouriet *et al.* [41] on the ultimate mechanical properties of forsterite shed light on the mechanical loss of stability of the olivine structure at the atomic scale. It can be seen that SiO_4 tetrahedra are not affected because of their ionocovalent bonds. The resistance of the structure depends mostly on the Mg–O bonds. In olivine there exists two magnesium sites named "Mg^1" and "Mg^2" (see [41]). The calculations show that the mechanical stability of the olivine structure depends ultimately on the resistance of Mg^2-O bonds. We can therefore see that amorphization exploits all the weak areas of the structure and this at any scale. These are the bonds at the scale of the unit cell with concentration of the strain on certain Mg-O bonds, or the crystal defects at

a higher scale. This is the case of grain boundaries as described by Samae *et al.* [30], and, inside the grains, along some particular lattice planes such as (010) which give rise to a preferential localized amorphization (Fig. 1d). Indeed, Gouriet et al. [41] calculations have shown that the lowest ideal shear stress corresponds to the (010) plane when it is sheared along [001]. The lowest ideal tensile stress also corresponds to a crystal pulled perpendicular to (010). These calculations explain the preferential alignment of some intragranular amorphous lamellae along the (010) plane, as seen in Fig. 1d.

5. Conclusion

Our characterization of an interrupted amorphization shear lamella in an olivine grain provide information on the stress-induced amorphization mechanism. The mechanical origin of the amorphization is indicated by the complex (and heterogeneous) shape of the displacement field which involves loading components in modes I, II and III. We show that amorphization is indeed accompanied by the formation of crystal defects, but in quantities and configuration that are not sufficient to be the cause of the mechanical instability. We rather interpret the formation of these defects (which are GNDs and possibly disclinations) as the evidence of very high stresses that drive the mechanical instability of the crystal structure. The formation of these defects underlines the complex pattern of the stress field which leads to amorphization. They strongly control the path followed by the propagating lamella. In some particular cases, the propagation of the amorphous lamella is very crystallographically controlled with a preference for the (010) plane which is indicative of the lower ultimate mechanical strength of these planes.

Declaration of Competing Interest

The authors declare that they have no known competing financial interests or personal relationships that could have appeared to influence the work reported in this paper.

Acknowledgement

The QuanTEM microscope was partially funded by the Flemish government. The K2 camera was funded by FWO Hercules fund G0H4316N 'Direct electron detector for soft matter TEM'. A. Béché acknowledges funding from FWO project G093417N ('Compressed sensing enabling low dose imaging in transmission electron microscopy'). H. Idrissi is mandated by the Belgian National Fund for Scientific Research (FSR- FNRS). This work was supported by the FNRS under Grant PDR – T011322F and by the European Research Council (ERC) under the European Union's Horizon 2020 research and innovation programme under grant agreement No 787,198 – TimeMan. J-L Rouviere is acknowledged for his support with the GPA softawre.

References

[1] I. Szlufarska, R. Kalia, A. Nakano, P. Vashishta, Nanoindentation-induced amorphization in silicon carbide, Appl. Phys. Lett. 85 (2004) 378, doi:10.1063/1.1774252.
[2] S. Zhao, R. Flanagan, E.N. Hahn, B. Kad, B.A. Remington, C.E. Wehrenberg, R. Cauble, K. More, M.A. Meyers, Shock-induced amorphization in silicon carbide, Acta Mat 158 (2018) 206–213, doi:10.1016/j.actamat.2018.07.047.
[3] M. Chen, J.W. McCauley, K.J. Hemker, Shock-Induced Localized Amorphization in Boron Carbide, Science 299 (2003) 1563–1566, doi:10.1126/science.1080819.
[4] G. Subhash, A.P. Awasthi, C. Kunka, P. Jannotti, M. DeVries, In search of amorphization-resistant boron carbide, Scripta Mater 123 (2016) 158–162, doi:10.1016/j.scriptamat.2016.06.012.
[5] D. Guo, S. Song, R. Luo, W.A. Goddard III, M. Chen, K.M. Reddy, Q. An, Grain Boundary Sliding and Amorphization are Responsible for the Reverse Hall-Petch Relation in Superhard Nanocrystalline Boron Carbide, Phys. Rev. Lett. 121 (2018) 145504, doi:10.1103/PhysRevLett.121.145504.
[6] K. Minowa, K. Sumino, Stress-Induced Amorphization of a Silicon Crystal by Mechanical Scratching, Phys. Rev. 69 (2) (1992) 320–322, doi:10.1103/PhysRevLett.69.320.
[7] Z.C. Li, L. Liu, X. Wu, L.L. He, Y.B. Xu, Indentation induced amorphization in gallium arsenide, Mat. Sci. Eng. A 337 (2002) 21–24, doi:10.1016/S0921-5093(02)00015-1.
[8] Y. He, L. Zhong, F. Fan, C. Wang, T. Zhu, S.X. Mao, In situ observation of shear-driven amorphization in silicon crystals, Nature Nanotech 11 (2016) 866–871, doi:10.1038/nnano.2016.166.
[9] S. Zhao, B. Li, B.A. Remington, C.E. Wehrenberg, H.S. Park, E.N. Hahn, M.A. Meyers, Directional amorphization of covalently-bonded solids: A generalized deformation mechanism in extreme loading, Materials Today 49 (2021) 59–67, doi:10.1016/j.mattod.2021.04.017.
[10] O. Mishima, L.D. Calvert, E. Whalley, Melting' ice I at 77 K and 10 kbar: a new method of making amorphous solids, Nature 310 (1984) 393–395.
[11] R.J. Hemley, A.P. Jephcoat, H.K. Mao, L.C. Ming, M.H. Manghnani, Pressure-induced amorphization of crystalline silica, Nature 334 (1988) 52–54, doi:10.1038/334052a0.
[12] P. Richet, P. Gillet, Pressure-induced amorphization of minerals: a review, Eur. J. Mineral. 9 (1997) 907–933.
[13] P.R. Okamoto, N.Q. Lam, L.E. Rehn, Physics of crystal-to-glass transformations, Solid State Phys 52 (1999) 1–135.
[14] M.M. Aleksandrova, V.D. Blank, A.E. Golobokov, Y.S. Konyaev, A.Y. Zerr, E.I. Estrin, Amorphisation of Gallium Antimonide under the Conditions of Shear Deformation under Pressure, Phys. Stat. Sol. (a) 105 (1988) K29–K32 http://dx.doi.org/10.1002/pssa.2211050141.
[15] M.Y. Gutkin, I.A. Ovid'ko, Plastic Flow in amorphous covalent solids and nanoceramics with amorphous intergranular layers, Rev. Adv. Mater. Sci. 21 (2009) 139–154.
[16] S.V. Bobylev, I.A. Ovid'ko, Nanoscale amorphization at disclination quadrupoles in deformed nanomaterials and polycrystals, Appl. Phys. Lett. 93 (2008) 061904 http://dx.doi.org/10.1063/1.2953448.
[17] Q. An, W.A. Goddard III, T. Cheng, Atomistic Explanation of Shear-Induced Amorphous Band Formation in Boron Carbide, Phys. Rev. Lett. 113 (2014) 095501, doi:10.1103/PhysRevLett.113.095501.
[18] H. Idrissi, P. Carrez, P. Cordier, On amorphization as a deformation mechanism under high stresses, Curr. Opin. Solid State Mater. Sci. 26 (2022) 100976, doi:10.1016/j.cossms.2021.100976.
[19] I.A. Ovid'ko, Nanoscale amorphization as a special deformation mode in nanowires, Scripta Mat 66 (2012) 402–405 http://dx.doi.org/10.1016/j.scriptamat.2011.12.001.
[20] S. Zhao, Z. Li, C. Zhu, W. Yang, Z. Zhang, D.E.J. Armstrong, P.S. Grant, R.O. Ritchie, M.A. Meyers, Amorphization in extreme deformation of the CrMnFeCoNi high-entropy alloy, Sci. Adv. 7 (5) (2021) eabb3108, doi:10.1126/sciadv.abb3108.
[21] J. Koike, D.M. Parkin, M. Nastasi, Crystal-to-amorphous transformation of NiTi induced by cold rolling, J. Mater. Res. 5 (7) (1990) 1414–1418, doi:10.1557/JMR.1990.1414.
[22] K.M. Reddy, A. Hirata, P. Liu, T. Fujita, T. Goto, M.W. Chen, Shear amorphization of boron suboxide, Scripta Mat 76 (2014) 9–12, doi:10.1016/j.scriptamat.2013.12.001.
[23] K.M. Reddy, D. Guo, S. Song, C. Cheng, J. han, X. Wang, Q. An, M. Chen, Dislocation-mediated shear amorphization in boron carbide, Sci. Adv. 7 (2021) eabc6714, doi:10.1126/sciadv.abc6714.
[24] Z.J. Lin, M.J. Zhuo, Z.Q. Sun, P. Veyssière, Y.C. Zhou, Amorphization by dislocation accumulation in shear bands, Acta Mat 57 (9) (2009) 2851–2857, doi:10.1016/j.actamat.2009.02.040.
[25] J.Y. Huang, H. Yasuda, H. Mori, Deformation-induced amorphization in ball-milled (BM) silicon, Phil. Mag. Lett. 79 (6) (1999) 305–314.
[26] Y.C. Wang, W. Zhang, L.Y. Wang, Z. Zhang, E. Ma, J. Li, Z.W. Shan, In situ TEM study of deformation-induced crystalline-to-amorphous transition in silicon, NPG Asia Materials 8 (2016) e291 http://dx.doi.org/10.1038/am.2016.92.
[27] H. Chen, V.I. Levitas, L. Xiong, Amorphization induced by 60◦ shuffle dislocation pileup against different grain boundaries in silicon bicrystal under shear, Acta Mater. 179 (2019) 287–295, doi:10.1016/j.actamat.2019.08.023.
[28] E. Tochigi, E. Zepeda-alarcon, H.-R. Wenk, A.M. Minor, In situ TEM observations of plastic deformation in quartz crystals, Phys. Chem. Minerals 41 (2014) 757–765, doi:10.1007/s00269-014-0689-6.
[29] H. Luo, H. Sheng, H. Zhang, F. Wang, J. Fan, J. Du, J.P. Liu, I. Szlufarska, Plasticity without dislocations in a polycrystalline intermetallic, Nature Comm 10 (2019) 3587, doi:10.1038/s41467-019-11505-1.
[30] V. Samae, P. Cordier, S. Demouchy, C. Bollinger, J. Gasc, S. Koizumi, A. Mussi, D. Schryvers, H. Idrissi, Stress-induced amorphization triggers deformation in the lithospheric mantle, Nature 591 (2021) 82–86, doi:10.1038/s41586-021-03238-3.
[31] R. Jeanloz, T.J. Ahrens, J.S. Lally, G.L. Nord, J.M. Christie, A.H. Heuer, Shock-Produced Olivine Glass: First Observation, Science 197 (4302) (1977) 457–459, doi:10.1126/science.197.4302.457.
[32] K. Kranjc, A.S. Thind, A.Y. Borisevich, R. Mishra, R.M. Flores, P. Skemer, Amorphization and plasticity of olivine during low-temperature micropillar deformation experiments, J. Geophys. Res. Solid Earth 125 (2020) e2019JB019242, doi:10.1029/2019JB019242.
[33] C. Bollinger, K. Marquardt, F. Ferreira, Intragranular plasticity vs. grain boundary sliding (GBS) in forsterite: microstructural evidence at high pressures (3.5-5.0 GPa), Am. Min. 104 (2) (2019) 220–231.

[34] J. Gasc, S. Demouchy, F. Barou, S. Koizumi, P. Cordier, Creep mechanisms in the lithospheric mantle Inferred from deformation of iron-free forsterite aggregates at 900-1200 °C, Tectonophysics 761 (2019) 16–30, doi:10.1016/j.tecto.2019.04.009.
[35] M.S. Paterson, et al., Rock deformation experimentation, in: A. Duba, et al. (Eds.), The Brittle-Ductile Transition in Rocks: the Head Volume, AGU, Washington D.C., 1990, pp. 187–194. Geophys. Monogr. Ser..
[36] M.A.G.M. Manthilake, N. Walte, D.J. Frost, A new multi-anvil press employing six independently acting 800 tonne hydraulic rams, High Pressure Res 32 (2012) 195–207.
[37] M.J. Hÿtch, E. Snoeck, R. Kilaas, Quantitative measurement of displacement and strain fields from HREM micrographs, Ultramicroscopy 74 (3) (1998) 131–146.
[38] J-L Rouviere, E. Sarigiannidou, Theoretical discussions on the geometrical phase analysis, Ultramicroscopy 106 (1) (2005) 1–17.
[39] O. Takahashi, Y. Tamenori, T. Suenaga, T. Ikeda-Fukazawa, J. Matsuno, A. Tsuchiyama, XANES spectra of forsterite in crystal, surface, and amorphous states, AIP Advances 8 (2018) 025107, doi:10.1063/1.5017245.
[40] L.A.J. Garvie, Can electron energy-loss spectroscopy (EELS) be used to quantify hydrogen in minerals from the O K edge? Am. Min. 95 (1) (2010) 92–97, doi:10.2138/am.2010.3290.
[41] K. Gouriet, P. Carrez, P. Cordier, Ultimate mechanical properties of forsterite, Minerals 9 (2019) 787, doi:10.3390/min9120787.